*Progress In Electromagnetics Research M, Vol. 69, 37–49, 2018*

# A Novel Hybrid Excitation Double-Stator Bearingless Switched Reluctance Motor

**Qian Wen Xiang*, Meng Jiao Fang, Ye Yuan, and Yanjun Yu**

**Abstract**—In view of lower power density and being unable to produce big radial force, this paper presents a new design of the hybrid excitation double-stator bearingless switched reluctance motor, which combines conventional double-stator bearingless switched reluctance motor (DSBSRM) with rare-earth permanent magnetic materials of high performance. Firstly, the basic structure and principle of the hybrid excitation DSBSRM are introduced. Secondly, the electromagnetic analysis is performed on the motor by two-dimensional finite element analysis (2D FEA), and the comparison is made between the proposed motor and traditional DSBSRM. Thirdly, the magnetic equivalent circuit (MEC) is established to deduce the mathematical models of the radial suspension force, torque and inductance. The current stiffness coefficient and displacement stiffness coefficient are derived by linearizing the mathematical models. Finally, the mathematical models are proved to be correct by 2D FEA.

## 1. INTRODUCTION

Switched reluctance motor (SRM) is a type of AC system which appears with the rapid development of power electronics and microelectronics [1]. The motor, which has a simple structure and big mechanical strength, can achieve rotation and energy conversion at the same time and be suitable for high-speed and ultra-high-speed operation [2]. However, the mechanical bearing reduces the efficiency and shortens the life span of the motor. The appearance of the magnetic bearing technology overcomes the shortcomings of mechanical bearings, which has no wearing, no friction, high precision and long service life [3]. However, magnetic bearings installed at both sides of motor increase the axial length and limit the critical speed [4]. To overcome these shortcomings, bearingless motors are used. In view of the stator similarity of SRM and magnetic bearing [5], suspension coils are wound in an SRM stator to form bearingless switched reluctance motor (BSRM), which combines the advantages of magnetic bearing and SRM. The BSRM, which has high axial utilization and high-speed operation, can be widely used in aerospace, flywheel energy storage and electric vehicles [6].

BSRM was first proposed by Chiba and other scholars in the 1990s [7]. Subsequently, large number of researches were done successively by scholars in different countries. Double windings BSRM was proposed in [8, 9], whose torque coils and suspension coils are wound at the same stator pole, achieving motor rotation and suspension at the same time, resulting in a strong coupling between the suspension force and the torque. The decoupling control was difficult and unpractical in industrial application. A type of single winding BSRM was introduced, whose stator pole coils were controlled independently [10]. It increases the power density, but the suspension force and torque is still coupled, and the controller is more complex. To decouple the suspension force and the torque, a hybrid stator type BSRM is proposed [11, 12]. The stator of the motor is composed of a wide stator pole to suspend rotor and a narrow stator pole to provide torque, which achieves an approximate decoupling between the suspension force and the torque. However, the coupling between radial two degrees of freedom is larger [13].

*Received 26 February 2018, Accepted 9 May 2018, Scheduled 29 May 2018*
* Corresponding author: Qian Wen Xiang (xqw@ujs.edu.cn).
The authors are with the School of Electrical and Information Engineering, Jiangsu University, Zhenjiang, Jiangsu 212013, China.

Therefore, a double-stator bearingless switched reluctance motor is proposed in [14, 15], in which the inner and outer stators are respectively wound with suspension force coils and torque coils, so as to effectively overcome the coupling between the torque and suspension force and between the suspension forces in two radial control degrees of freedom [16, 17]. However, the power density of the control current is small, and the expense of the same suspension force produced is increased due to the inner-stator size limitations.

In this paper, the idea of "hybrid excitation" is introduced into DSBSRM, and a new hybrid excitation double-stator bearingless switched reluctance motor is proposed. The permanent magnet is embedded in the inner stator, and the permanent magnet cooperates with the control current to provide levitation force. The paper first describes the structure and working principle of the proposed motor. Secondly, the electromagnetic characteristics are analyzed by 2D FEA. Then, the mathematical models of the torque, inductance and suspension force are deduced by the MEC. Finally, these models are proved correct by 2D FEA.

## 2. TOPOLOGY OF THE PROPOSED MOTOR

The hybrid excitation bearingless switched reluctance motor is shown in Fig. 1, whose stator and rotor have salient poles. The rotor has no coils and no permanent magnet. The outer stator has three-phase concentrated coils to produce torque. Torque coils A1, A2, A3, A4 are connected in series to form phase A.

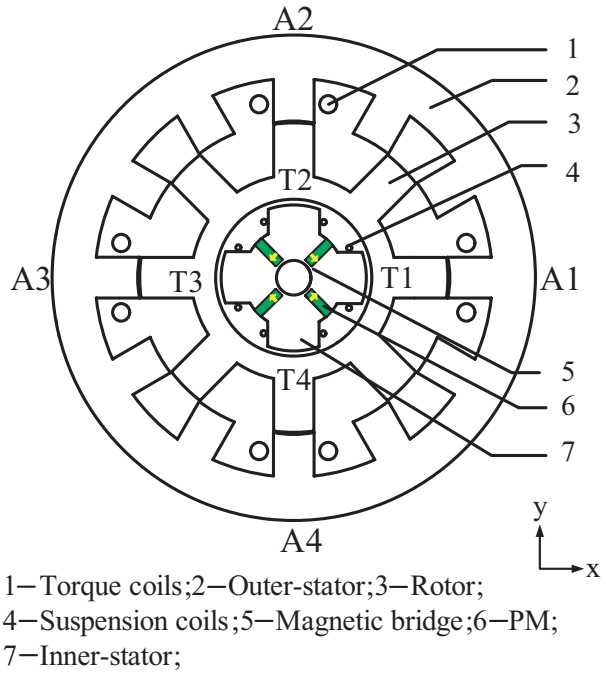


**Figure 1.** Schematic diagram.

Four tangentially magnetized permanent magnets are embedded in the inner stator. A certain size of the magnetic bridge is set between the permanent magnet and the shaft. On the one hand, the inner stator is not divided into blocks and maintains a whole, which is conductive to manufacture. On the other hand, the magnetic bridge provides a magnetic flux path for the suspension coils and reduces the risk of demagnetization of the permanent magnet. Suspension coils T1, T2, T3, T4 are placed in the inner stator, where T1 and T3 are connected in series to provide control flux in the $x$-axis direction. T2 and T4 are connected in series to provide control flux in the $y$-axis direction.

## 3. PRINCIPLE OF THE PROPOSED MOTOR

The torque of the proposed motor is generated by the outer stator and rotor, as shown in Fig. 2(a). Its working principle is similar to the switched reluctance motor, following the "minimum principle of reluctance", which means that the magnetic flux generated by the torque current always follows the path of the minimum magnetic reluctance. Due to tangential magnetic force produced from distorted flux, the rotor starts to rotate.

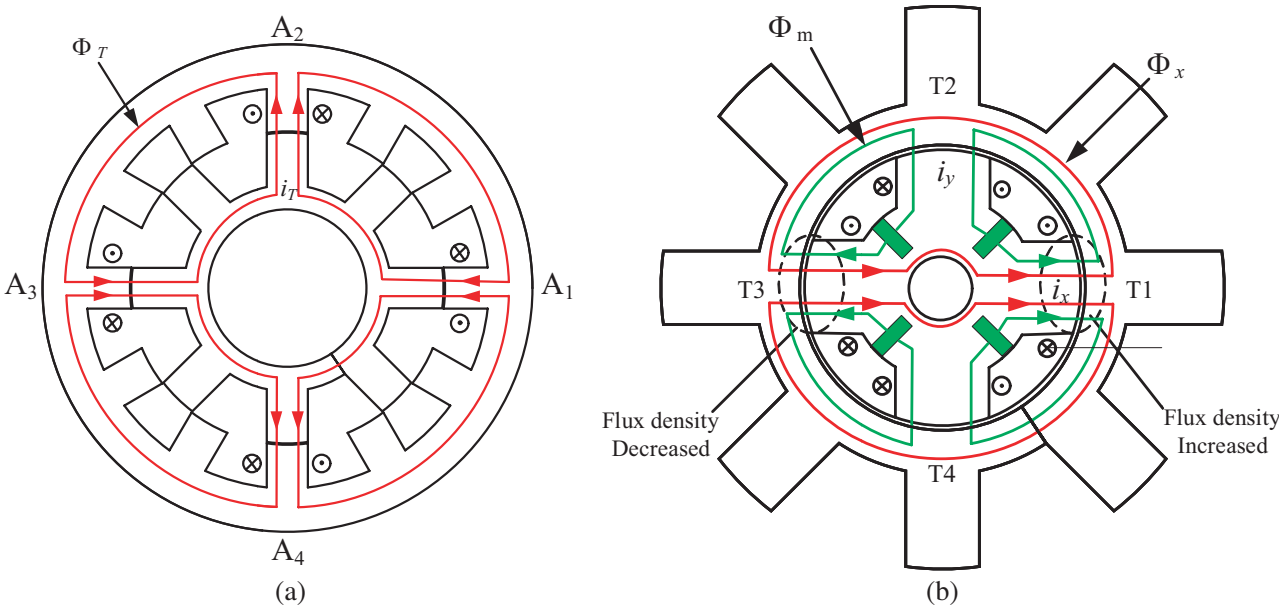


**Figure 2.** Operation principle. (a) Torque. (b) Suspension force.

The generation of radial suspension force is shown in Fig. 2(b), which is the result of the combination of the permanent magnet and inner-stator suspension coils. When the rotor is at a balanced position, the magnetic field produced by the permanent magnet is evenly distributed in the air gap. When the rotor is disturbed in $+x$ direction, the rotor will move away from the center to $+x$ direction, whose air gap becomes larger, and magnetic flux $\Phi_m$ generated by the permanent magnet decreases. Then, the attraction force of permanent magnet decreases. In the $-x$ direction, $\Phi_m$ increases, and the magnetic attraction force increases. At this time, the sensor detects the eccentricity; the controller changes the displacement signal into a control signal; the power amplifier transforms the control signal into a control current which flows through the coil to generate magnetic flux. Therefore, the magnetic flux increases in $+x$ direction, and the magnetic flux decreases in $-x$ direction. The suspension force in $+x$ direction is generated to make the rotor in the center.

## 4. ELECTROMAGNETIC ANALYSIS

### 4.1. Finite Element Analysis

The finite element analysis is performed by Ansoft Maxwell software which can calculate magnetic potential of the node. The 2D FEA model of the motor is given in Fig. 3. Due to the existence of current source in the solving region, the magnetic potential is used to solve the calculation.

In order to build magnetic field and determine the solving region and boundary conditions for finite element method, there are some assumptions.

1) The end effect is neglected, and the magnetic field is distributed along the $z$-axial direction uniformly. Therefore, the current density vector and magnetic vector potential are expressed by axial component $J_z$ and $A_z$, respectively.

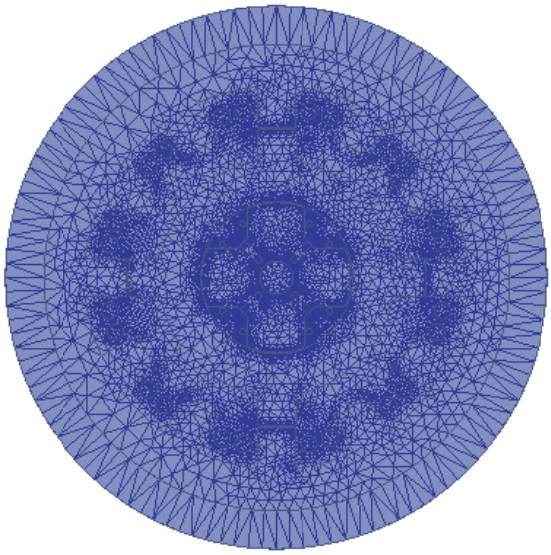

**Figure 3.** 2D FEA model in Maxwell.

2) The rotor is located at the center of the shaft. The radial displacement of rotor is not considered during the finite element analysis.
3) The external magnetic field of the motor is ignored.

The $z$-axial component of magnetic vector potential $A_z(x, y)$ is expressed as:

$$J_z(x, y) = \nabla \times \left( \frac{1}{\mu_r \mu_0} (\nabla \times A_z(x, y)) \right) \tag{1}$$

where $J_z(x, y)$ is the current density vector of the cross section, $\mu_r$ the relative permeability of the material, $\mu_0$ the permeability of vacuum, and $x$ and $y$ are the radial displacements.

According to Maxwell equations, magnetic density $B$ and magnetic field intensity $H$ can be expressed as:

$$B = \nabla \times A \tag{2}$$

$$H = \frac{B}{\mu_r \mu_0} \tag{3}$$

The magneto-static torque is calculated by the principle of virtual work in Maxwell, which can be represented as:

$$T_B = \left. \frac{dW}{d\theta} \right|_{i=\text{const}} = \frac{\partial}{\partial \theta} \left[ \int_V \left( \int_0^H B \cdot dH \right) dV \right] \tag{4}$$

where $W$ is the magnetic co-energy, $\theta$ the rotor angle, and $i$ the constant current.

Similarly, magneto-static force is also calculated by the principle of virtual work in Maxwell and can be represented as:

$$F = \left. \frac{dW}{dx} \right|_{i=\text{const}} = \frac{\partial}{\partial x} \left[ \int_V \left( \int_0^H B \cdot dH \right) dV \right] \tag{5}$$

### 4.2. Coupling between Torque and Radial Force

In order to study the characteristics of the proposed motor, the two-dimensional finite element analysis model was established. The main parameters of the motor are listed in Table 1.

**Table 1.** Dimensions of hybrid excitation DSBSRM.

| Parameters | Value |
|---|---|
| Outer-stator Outer Diameter/mm | 112 |
| Outer-stator Inner Diameter/mm | 72 |
| Outer-stator yoke thickness/mm | 10 |
| Rotor Outer Diameter /mm | 71.4 |
| Rotor yoke thickness/mm | 12 |
| Rotor Inner Diameter/mm | 35 |
| Inner-stator Outer Diameter/mm | 34.2 |
| Inner-stator Inner Diameter/mm | 8 |
| PM Height/mm | 6.7 |
| PM Length/mm | 2 |
| Br of PM/T | 1.2 |

Based on the 2D FEA, the magnetic flux distribution of the PM and electric excitation is shown in Fig. 3. The magnetic flux produced by suspension coils is shown in Fig. 4(a), which flows through the inner-stator pole, the air gap and the rotor. It does not pass through the outer stator. Due to the large magnetic reluctance of the PM and the existence of magnetic bridge, the magnetic flux produced by suspension coils does not penetrate through the PM. The magnetic flux produced by torque coils is shown in Fig. 4(b), which flows through the yoke of outer stator, the pole of outer-stator, the air gap and the rotor. It can be seen that the magnetic flux does not penetrate the inner stator. The combinative magnetic flux of electric excitation and PM is shown in Fig. 4(c). It can be seen that the flux paths of the torque coils and suspension coils are independent from each other.

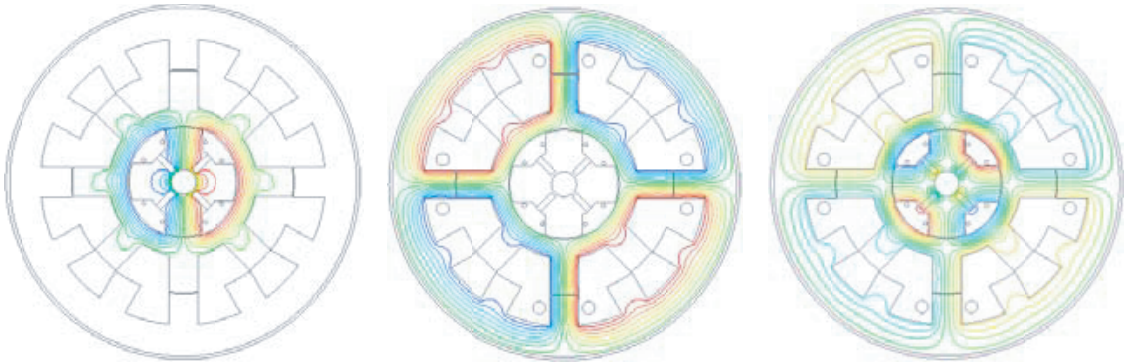

(a) (b) (c)

**Figure 4.** Flux distribution diagram. (a) Magnetic flux of suspension coils. (b) Magnetic flux of torque coils. (c) The combinative magnetic flux.

The new hybrid excitation DSBSRM has decoupled torque and suspension force, as shown in Fig. 5, where $F_y$ is the radial suspension force along the $y$-axis, $T$ the torque, $\theta_r$ the rotor angle, $i_y$ the suspension current along the $y$-axis, and $i_T$ the torque current of phase A. When the outer-stator poles of phase A are aligned to the rotor poles as shown in Fig. 1, defining $\theta_r = 0°$. The conduction angle of phase A is 15°.

When $i_T = 0$ A and $i_y$ varies from 1 A to 4 A, the relation between $T$ and $\theta_r$ is shown in Fig. 5(a). With $i_y$ changing the maximum torque produced by $i_y$ is less than 0.01 Nm. So, the suspension force current can hardly produce torque. When $i_y = 0$ A and $i_T$ varies from 1 A to 4 A, the relation between

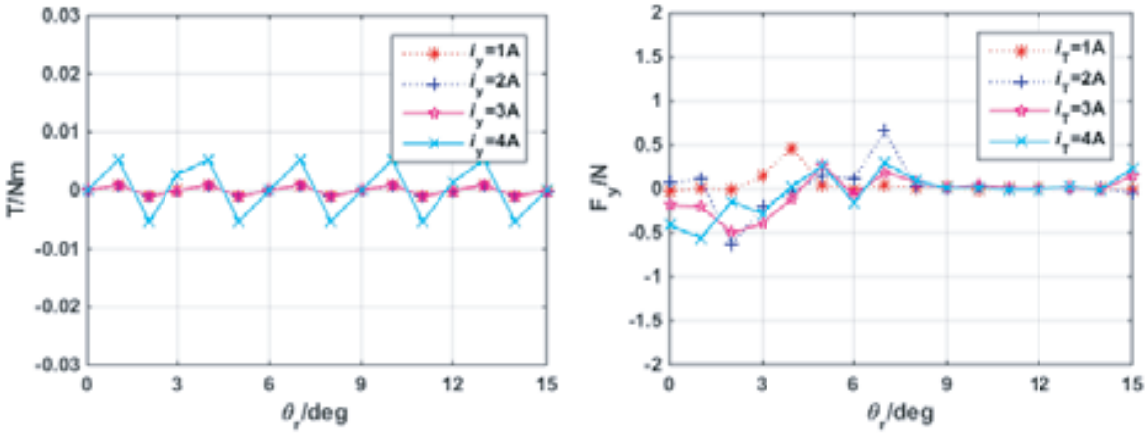


**Figure 5.** The coupling between torque and radial force. (a) $T$ versus $\theta_r$. (b) $F_y$ versus $\theta_r$.

$F_y$ and $\theta_r$ is shown in Fig. 5(b). With $i_T$ changing, the maximum suspension force produced by $i_T$ is less than 1 N. The torque current can hardly produce suspension force. Therefore, the coupling between the suspension force and the torque is slight and can be neglected.

### 4.3. Two Degrees Freedom Radial Force Coupling

The coupling characteristics between $F_x$ and $F_y$ is shown in Fig. 6. When $i_x = 0$ and $i_y$ varies from 1 A to 4 A, the $x$-axis suspension force $F_x$ is shown in Fig. 6(a). It can be seen that $F_x$ is almost zero. When $i_y = 0$ and $i_x$ varies from 1 A to 4 A, the relation between $F_y$ and $\theta_r$ is shown in Fig. 6(b). It can be seen that $F_y$ is less than 0.1 N. It is proved that the coupling between $F_x$ and $F_y$ is slight and can be neglected.

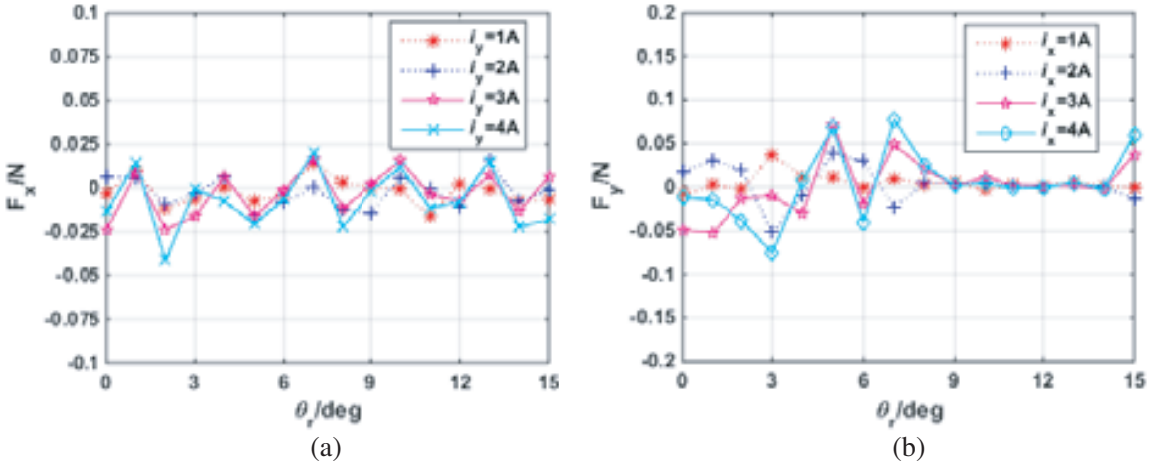


**Figure 6.** Two degrees freedom suspension force. (a) $F_x$ versus $\theta_r$. (b) $F_y$ versus $\theta_r$.

### 4.4. Comparison of Characteristics

Since suspension force is generated by the inner stator whose size is limited, the levitation force generated by the electric excitation is small. Therefore, a permanent magnet is added in the inner stator to increase magnetic attraction force at the same current. The performance comparison between traditional electric excitation DSBSRM and hybrid excitation DSBSRM at the same current is shown in Fig. 7. When

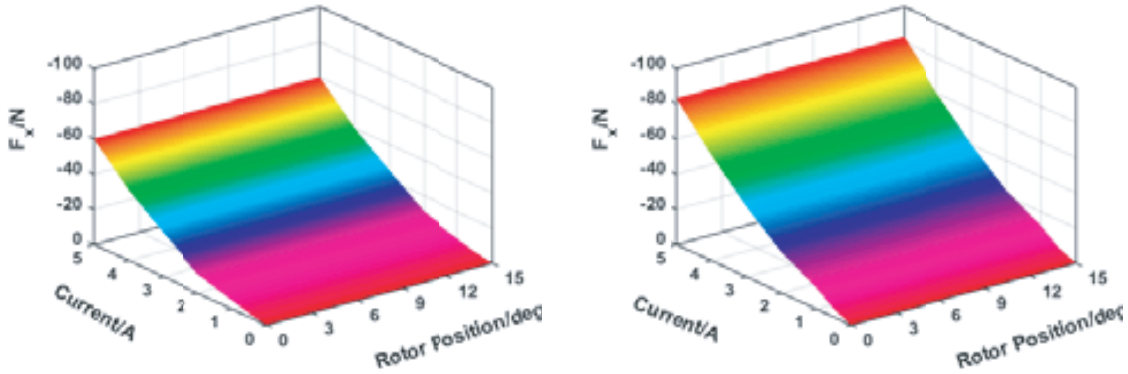


**Figure 7.** Comparison of the suspension force. (a) Traditional DSBSRM. (b) Hybrid excitation DSBSRM.

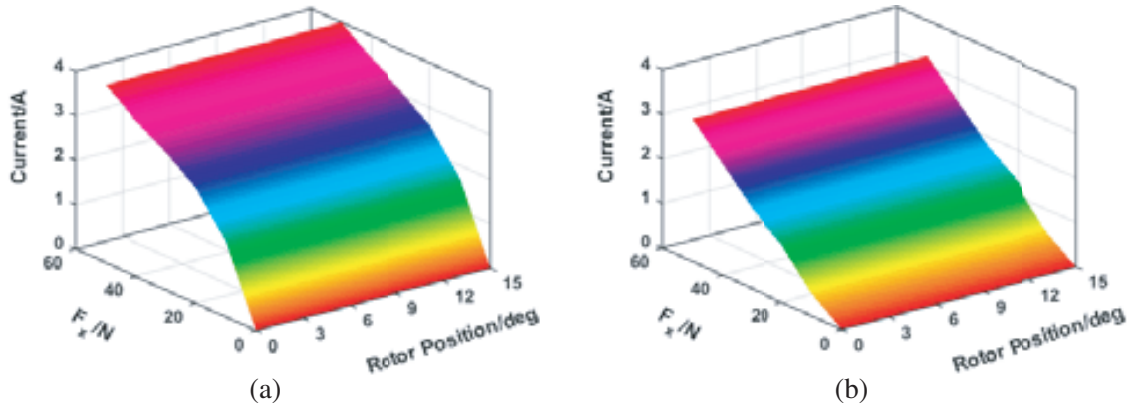


**Figure 8.** Comparison of the suspension current. (a) Traditional DSBSRM. (b) Hybrid excitation DSBSRM.

the suspension current varies from 0 A to 5 A, the suspension force of the hybrid excitation motor is 44.7% larger than that of the traditional motor on average. The change rate first increases and then decreases. The decrease is mainly due to the magnetic saturation in magnetic bridge where both the leakage flux and control flux pass through. Fig. 8 is the current comparison between above two motors under the same suspension force. The current of hybrid excitation DSBSRM can be reduced by nearly 30% on average. Therefore, hybrid excitation DSBSRM can reduce the power loss and improve radial load capacity.

## 5. MATHEMATICAL MODEL

### 5.1. Equivalent Magnetic Circuit

Due to the magnetic flux of the PM and control current in Fig. 4, the simplified MEC of biased and control flux is given. In this hybrid excitation BSRM, due to the large magnetic reluctance of the PM and the existence of magnetic bridge, the control flux does not penetrate through the permanent magnet as shown in Fig. 4(a). It can be considered that the bias flux has parallel connection with control flux. We can build the bias magnetic circuit model and control magnetic circuit model separately as shown in Fig. 9.

$F_m$ is the total external magnetomotive force provided by the permanent magnet; $\phi_{c1} \sim \phi_{c4}$ are the radial bias flux; $R_m$ is the leakage resistance of the PM; $R_{c1} \sim R_{c4}$ are the air gap reluctance of bias magnetic flux produced by the PM; $Ni_x$ and $Ni_y$ are the magnetomotive force of the suspension

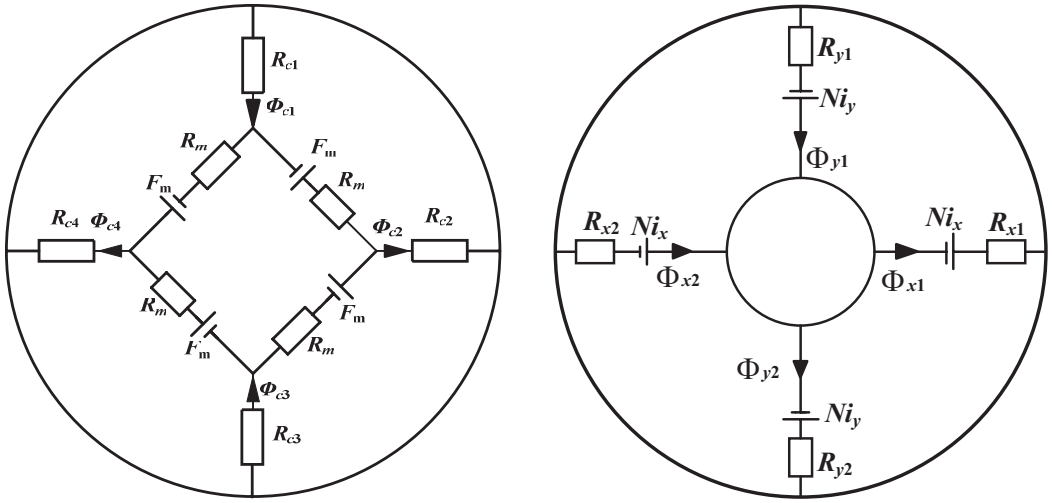


**Figure 9.** Simplified MEC of the biased and control flux. (a) Biased flux. (b) Control flux.

coils in the $x$-axis and $y$-axis, respectively; $N$ is the turns of the suspension coils; $\phi_{x1}, \phi_{x2}, \phi_{y1}, \phi_{y2}$ are the control flux; $R_{x1}, R_{x2}, R_{y1}, R_{y2}$ are air-gap resistance of the suspension coils. Based on the above magnetic circuit, the air gap reluctance $R$ can be approximated as:

$$\begin{cases} R_{x1} = \dfrac{g_0 + x}{\mu_0 S_{xy}} \\ R_{x2} = \dfrac{g_0 - x}{\mu_0 S_{xy}} \\ R_{y1} = \dfrac{g_0 + y}{\mu_0 S_{xy}} \\ R_{y2} = \dfrac{g_0 - y}{\mu_0 S_{xy}} \end{cases} \tag{6}$$

where $g_0$ is the air gap length, $S_{xy}$ the control pole area, and $x$ and $y$ are the radial eccentricity.

According to the Kirchhoff's magnetic circuit, the biased magnetic flux can be obtained as:

$$\begin{cases} \phi_{c1} = \dfrac{(F_m/\varepsilon_b)(R_1R_4 + R_1R_2)}{R_1 + R_2 + R_3 + R_4} \\ \phi_{c2} = \dfrac{(F_m/\varepsilon_b)(R_2R_3 + R_1R_2)}{R_1 + R_2 + R_3 + R_4} \\ \phi_{c3} = \dfrac{(F_m/\varepsilon_b)(R_3R_4 + R_1R_3)}{R_1 + R_2 + R_3 + R_4} \\ \phi_{c4} = \dfrac{(F_m/\varepsilon_b)(R_3R_4 + R_1R_4)}{R_1 + R_2 + R_3 + R_4} \end{cases} \tag{7}$$

where $\varepsilon_b$ is the leakage coefficient of the PM, and $R_1 = 1/R_{c1}$, $R_2 = 1/R_{c2}$, $R_3 = 1/R_{c3}$, $R_4 = 1/R_{c4}$. $\varepsilon_b$ can be obtained from the leakage resistance $R_m$.

The control flux can be obtained as:

$$\begin{cases} \phi_{x1} = \phi_{x2} = \dfrac{\mu_0 S_{xy} N i_x}{\varepsilon_c g_0} \\ \phi_{y1} = \phi_{y2} = \dfrac{\mu_0 S_{xy} N i_y}{\varepsilon_c g_0} \end{cases} \tag{8}$$

where $\varepsilon_c$ is the leakage coefficient of the control flux.

### 5.2. Radial Suspension Force

Based on above magnetic circuit and according to the principle of Maxwell stress tensor, the suspension force can be deduced as:

$$\begin{cases} F_x = \dfrac{(\phi_{x1}+\phi_{c2})^2-(\phi_{c4}-\phi_{x2})^2}{2\mu_0 S_{xy}} \\ F_y = \dfrac{(\phi_{y1}+\phi_{c1})^2-(\phi_{c3}-\phi_{y2})^2}{2\mu_0 S_{xy}} \end{cases} \tag{9}$$

Linearizing near the center position and neglecting the infinitesimal second order:

$$\begin{aligned} F_{x,y} &= \left.\frac{\partial F_{x,y}}{\partial x,y}\right|_{\substack{x=y=0\\ i_x=i_y=0}} (x,y) + \left.\frac{\partial F_{x,y}}{\partial x,y}\right|_{\substack{x=y=0\\ i_x=i_y=0}} (i_x,i_y) \\ &= K_{x,y}(x,y) + K_{i_x,i_y}(i_x,i_y) \end{aligned} \tag{10}$$

where $K_{x,y}$ is the displacement stiffness coefficient, and $K_{i_x,i_y}$ is the current stiffness coefficient.

$$\begin{cases} K_{x,y} = \dfrac{3F_m^2\mu_0 S_{xy}}{8\varepsilon_b^2 g_0^3} \\ K_{i_x,i_y} = \dfrac{F_m\mu_0 N S_{xy}}{\varepsilon_b\varepsilon_c g_0^2} \end{cases} \tag{11}$$

### 5.3. Torque

Ignoring the higher harmonic wave of phase inductance, the phase inductance of the torque coils can be written as:

$$L(\theta) = L_0 + L_1\cos(N_r\theta_r+\pi) \tag{12}$$

$$\begin{cases} L_0 = \dfrac{L_{\max}(i_T)+L_{\min}(i_T)}{2} \\ L_1 = \dfrac{L_{\max}(i_T)-L_{\min}(i_T)}{2} \end{cases} \tag{13}$$

where $L_{\min}$ is the minimum inductance, $L_{\max}$ the maximum inductance, and $N_r$ the number of rotor poles.

When the rotor salient pole coincides with the outer-stator groove center, the magnetic circuit works at an unsaturated state, and the inductance is minimized. Therefore, $L_{\min}$ does not change with the phase current and can be considered as a constant. When $\theta_r = 0°$, the inductance reaches its maximum $L_{\max}$, which can be expressed as $L_{\max}$=$f(i_T)$.

The inductance value can be obtained by 2D FEA, where $L_{\min}$ is 0.028 H, and $L_{\max}$=$f(i_T)$ is shown in Fig. 10.

Using the least-square method to fit these simulation data segmentally, we can obtain $L_{\max}$ as:

$$L_{\max}(i_T) = \begin{cases} -0.0011i_T^2+0.0028i_T+0.2593 & i_T \le 3 \\ -0.0016i_T+0.2627 & i_T > 3 \end{cases} \tag{14}$$

Substituting Equation (14) into Equations (12) and (13), the inductance can be expressed as:

$$L(\theta_r,i_T) = \begin{cases} (-0.00055i_T^2+0.0014i_T+0.144)+(-0.00055i_T^2+0.0014i_T+0.116)\cos(N_r\theta_r+\pi) \\ i_T \le 3 \\ (-0.0008i_T+0.1454)+(-0.0008i_T+0.12)\cos(N_r\theta_r+\pi) \\ i_T > 3 \end{cases} \tag{15}$$

According to the principle of virtual displacement, torque $T_{ek}$ can be calculated as:

$$T_{ek} = \frac{\partial W'(i_T,\theta_r)}{\partial\theta_r} = \frac{\partial\int_0^{i_T} L_k(i_T,\theta_r)i_T di_T}{\partial\theta_r} \tag{16}$$

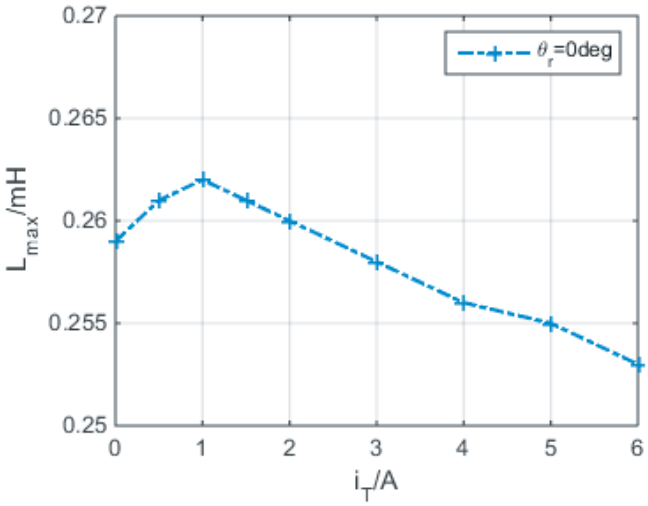


**Figure 10.** The relationship between $L_{\max}$ and $i_T$.

By substituting formula (15) into formula (16), the torque $T_{ek}$ can be further calculated as:

$$T_{ek} = \begin{cases} \left(0.0001375i_T^4 - 0.00047i_T^3 - 0.058i_T^2\right) N_r \sin\left[N_r\theta_r + \pi\right] & i_T \le 3 \\ -0.34N_r \sin\left(N_r\theta_r + \dfrac{(5-2k)}{3}\pi\right) + \left(0.0008i_T^2 - 0.265i_T\right) N_r \sin\left[N_r\theta_r + \pi\right] & i_T > 3 \end{cases} \tag{17}$$

## 6. FINITE ELEMENT SIMULATION VERIFICATION

Based on the 2D FEA model in Fig. 3, the mathematical models deduced in Section 5 can be verified.

According to formula (10), the radial suspension force can be calculated. The relation between the suspension force and suspension current is shown in Fig. 11(a). When $i_y$ varies from 0 A to 10 A, the suspension force maximum error is only about 3.9%, which is in the acceptable region. Fig. 11(b) is the relation between the suspension force and the rotor radial eccentricity. When the eccentricity varies

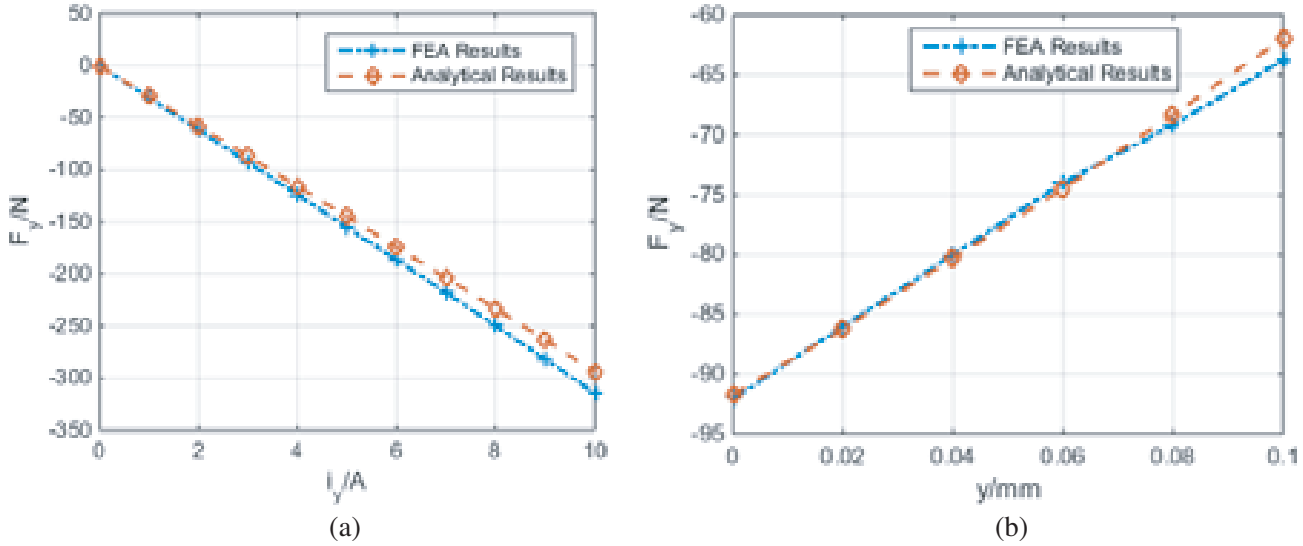


**Figure 11.** Suspension force verification of hybrid excitation DSBSRM. (a) $F_y$ versus $i_y$. (b) $F_y$ versus $y$.

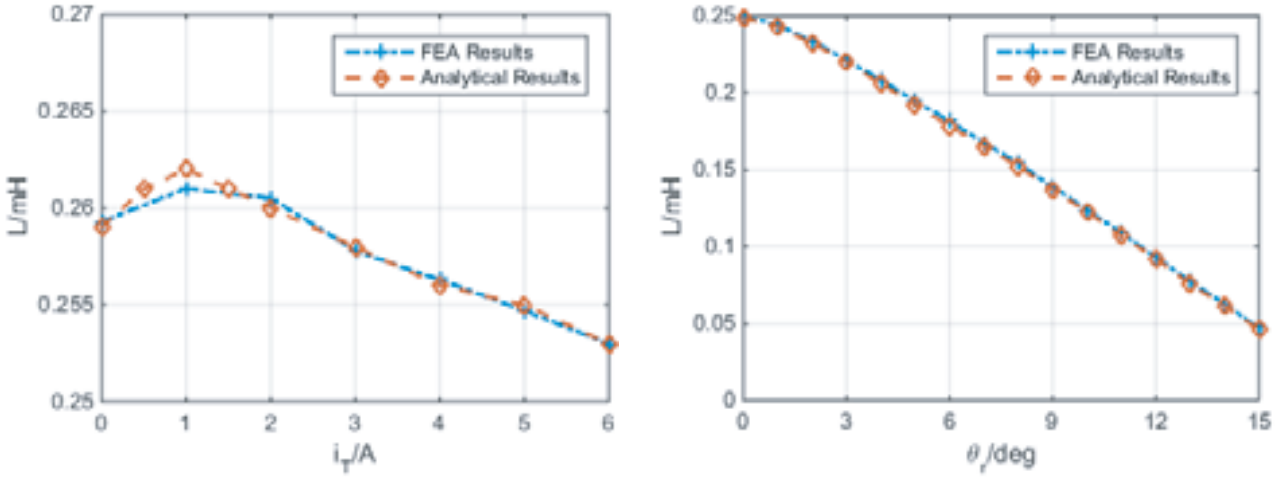


(a) (b)

**Figure 12.** Inductance verification of hybrid excitation DSBSRM. (a) $L$ versus $i_T$. (b) $L$ versus $\theta_r$.

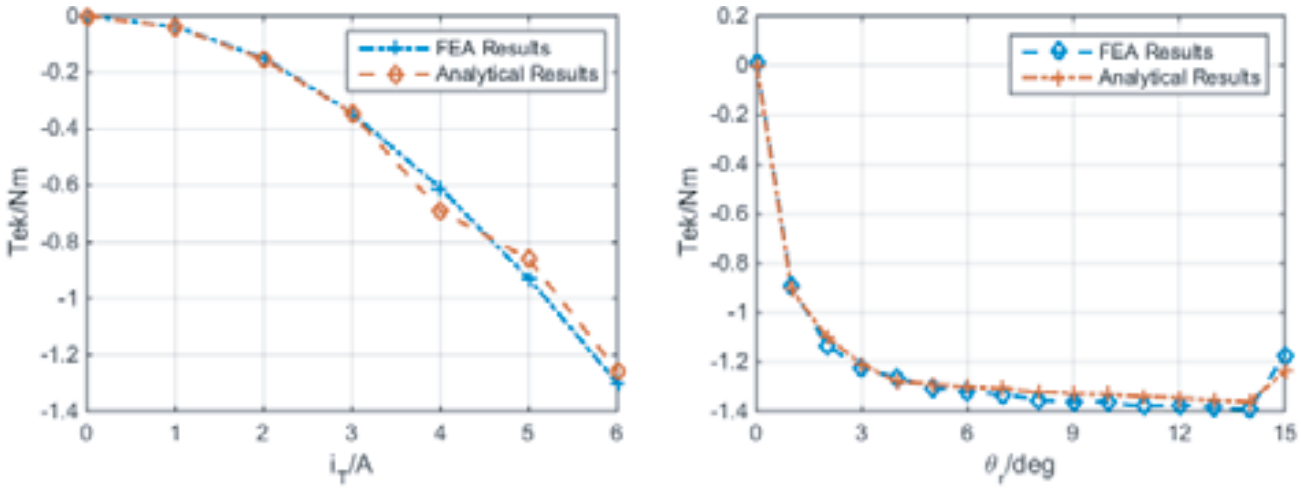


(a) (b)

**Figure 13.** Torque verification of hybrid excitation DSBSRM. (a) $T$ versus $i_T$. (b) $T$ versus $\theta_r$.

from 0 to 0.1 mm, the maximum error of the suspension force is 4.1% at 0.1 mm. It can be seen that the theoretical value is close to the calculated value of FEA, when current and eccentricity are small. With the current and eccentricity increasing, the theoretical value is slightly larger than the FEA result due to the impact of magnetic flux leakage and magnetic saturation. According to the analysis, the theoretical results are basically consistent with the FEA results.

According to formula (15), the inductance of phase A can be calculated. Fig. 12(a) is the curve of the inductance $L$ versus $i_T$ at $\theta_r = 0°$. It can be seen that the analytical results are basically consistent with the FEA results. We can also see that the inductance rate declines with increasing $i_T$ because of the magnetic saturation. Fig. 12(b) shows the curve of the inductance $L$ versus $\theta_r$ at $i_T = 2$ A. The inductance decreases gradually with the rotor rotating. The analytical results agree well with the FEA ones.

According to formula (17), the torque can be calculated. Fig. 13(a) is the curve of torque versus $i_T$ at $\theta_r = 7.5°$ The maximum error between formula (17) and FEA is 8.9% at 4 A, which is in the accepted region. Fig. 13(b) is the curve of torque versus $\theta_r$ at $i_T = 2$ A. It can be seen that the analytical results are basically consistent with the FEA ones.

## 7. CONCLUSION

This paper presents a hybrid excitation double-stator bearingless switched reluctance motor, stating its structure and working principle, and then presenting electromagnetic characteristics of the proposed motor.

Comparison is made between traditional DSBSRM and the proposed motor. The mathematical models are established based on the MEC and then verified by 2D FEA. Based on the analysis, the proposed motor has following advantages:

(1) The proposed hybrid excitation DSBSRM improves the radial suspension force under the same conditions and decreases the suspension current when the same radial force is produced.

(2) The Magnetic bridge is added between the PM and the shaft. On the one hand, it makes the inner stator a whole, which is convenient for machining. On the other hand, it provides a path for the magnetic flux excited by the suspension current and reduces the risk of demagnetization of the PM.

(3) During the rotation, the radial suspension force does not change with the rotor angle, so as to overcome the problem that the traditional BSRM cannot produce enough suspension force at some special rotor positions.

(4) The proposed motor has excellent decoupling characteristics between the torque and the suspension force. Meanwhile, the mutual influence between two degrees freedom radial force can be ignored.

## ACKNOWLEDGMENT

Project Supported by the Natural Science Foundation of Jiangsu Province (BK 20150510; BK 20170546), Project Funded by Senior Talent Research Funding of Jiangsu University (14JDG075), and National Natural Science Foundation of China (51707082).

## REFERENCES

1. Pollock, H., C. Pollock, R. T. Walter, et al., "Low cost high power density, flux switching machines and drives for power tools," *IEEE IAS Annual Meeting*, 132–137, 2003.
2. Wang, J. H., *Design and Application of Switched Reluctance Motor*, Machinery Industry Press, 2000 (in Chinese).
3. Eryong, H. and L. Kun, "Investigation of axial carrying capacity of radial hybrid magnetic bearing," *IEEE Transactions on Magnetics*, Vol. 48, No. 1, 38–46, 2011.
4. Han, B., S. Zheng, Y. Wang, et al., "A FEM-Based method dynamic analysis of a thrust magnetic bearing with permanent magnet bias," *IEEE International Symposium on Instrumentation and Control Technology*, 281–285, 2012.
5. Takemoto, M., A. Chiba, H. Akagi, et al., "Radial force and torque of a bearingless switched reluctance motor operating in a region of magnetic saturation," *IEEE Transactions on Industry Application*, Vol. 40, No. 1, 103–112, 2004.
6. Deng, Z. Q., G. Yang, et al., "A novel mathematical model of bearingless switched reluctance motor," *Proceeding of the CSEE*, Vol. 25, No. 9, 139–146, 2005 (in Chinese).
7. Takemoto, M., K. Shimada, A. Chiba, et al., "A design and characteristics of switched reluctance type bearingless motors," *Proc. NASA/CP*, 49–63, 1998.
8. Takemoto, M., K. Shimada, A. Chiba, et al., "A design and characteristics of switched reluctance type bearingless motors," *Proceeding of the 4th International Transactions on Industrial Electronics*, 2592–2600, 2012.
9. Kabir, M. A. and I. Husain, "Design of mutually coupled switched reluctance motors (MCSRMs) for extended speed applications using 3-phase standard inverters," *IEEE Transactions on Energy Conversion*, Vol. 31, No. 2, 436–445, 2016.
10. Lin, F.-C. and S.-M. Yang, "An approach to producing controlled radial force in a switched reluctance motor," *IEEE Transactions on Industrial Electronics*, Vol. 54, No. 4, 2137–2146, 2007.

11. Chen, L. and W. Hofmann, "Speed regulation technique of one bearingless 8/6 switched reluctance motor with simpler single winding structure," *IEEE Transactions on Industrial Electronics*, Vol. 59, No. 6, 2592–2600, 2012.
12. Z. Xu, F. Zhang, D. H. Lee, and J. W. Ahn, "Design and analysis of novel 12/14 hybrid pole type bearingless switched reluctance motor with short flux path," *Journal of Electrical Engineering and Technology*, Vol. 7, No. 5, 705–713, 2012
13. Lee, D. H., H. J. Wang, and J. W. Ann, "Modeling and control of novel bearingless switched reluctance motor," *IEEE Energy Conversion Congress and Exposition*, 276–281, 2009
14. Zhou, Y. and Y. Sun, "A double-stator bearingless switched reluctance motor double channel full cycle generator," *Proceedings of the CSEE*, Vol. 35, No. 9, 2295–2303, 2015 (in Chinese).
15. Zhou, Y. and Y. Sun, "Principle and implements of a double-stator bearingless switched reluctance starter/generator," *Proceedings of the CSEE*, Vol. 34, No. 36, 6458–6466, 2014 (in Chinese).
16. Sun, Y., et al., "A double-stator bearingless switched reluctance motor channel full cycle generator," *Proceedings of the CSEE*, Vol. 21, No. 1, 59–68, 2017 (in Chinese).
17. Liu, Z., Z. Q. Deng, and X. Chen, "Top-Ology and decoupling analysis of bearingless switched reluctance motor," *Journal of Nanjing Aeronautics and Astronautics*, Vol. 48, No. 5, 732–740, 2016 (in Chinese).